Paleoceanography and Paleoclimatology

RESEARCH ARTICLE
10.1029/2021PA004293

Semi-Automatic Ice-Rafted Debris Quantification With Computed Tomography

Jan Magne Cederstrøm[1], Willem G. M. van der Bilt[1], Eivind W. N. Støren[1], and Sunniva Rutledal[1]

[1]Department of Earth Science, University of Bergen, Norway and Bjerknes Centre for Climate Research, Bergen, Norway

Key Points:

- CT counting reproduces the known number of particles added to phantom archives
- CT counting tracks the main trends in published IRD profiles from sediment archives
- CT counting improves the sampling resolution to resolve higher-frequency variability

Supporting Information:

Supporting Information may be found in the online version of this article.

Correspondence to:

W. G. M. van der Bilt,
willemvanderbilt@uib.no

Citation:

Cederstrøm, J. M., van der Bilt, W. G. M., Støren, E. W. N., & Rutledal, S. (2021). Semi-automatic ice-rafted debris quantification with computed tomography. *Paleoceanography and Paleoclimatology*, *36*, e2021PA004293. https://doi.org/10.1029/2021PA004293

Received 29 APR 2021
Accepted 2 SEP 2021

Abstract Sedimentary ice-rafted debris (IRD) provides critical information about the climate sensitivity and dynamics of ice sheets. In recent decades, high-resolution investigations have revealed ice rafting events in response to rapid warming: such reconstructions help us constrain the near-future stability of our planet's fast-changing cryosphere. However, similar efforts require laborious and destructive analytical procedures to separate and count IRD. Computed tomography (CT) holds great promise to overcome these impediments to progress by enabling the micrometer-scale (max. ~21 μm) visualization of individual IRD grains. This study demonstrates the potential of this emerging approach by (a) validating CT counts in synthetic sediment archives (phantoms) spiked with a known number of grains, (b) replicating published IRD stratigraphies, and (c) improving sampling resolution. Our results show that semi-automated CT counting of grains in the often analyzed 150–500 μm size fraction reproduces grain numbers and tracks manually counted trends. We also find that differences between manual and CT-counted data are explained by image processing artifacts, offsets in sampling resolution, and bioturbation. By acquiring these promising results using basic image processing tools, we argue that our work advances and broadens the applicability of ultra-high resolution IRD counting with CT to deepen our understanding of ice sheet-climate interactions on human-relevant timescales.

Plain Language Summary Chunks of ice regularly break off glaciers floating in the ocean. These icebergs contain rock fragments and mineral grains picked up during the journey from land to water. As icebergs drift into warmer waters and melt, this rubble sinks to the bottom and settles on the ocean floor. Detection of these particles in marine sediments thus provides evidence that glacial ice reached down to sea level. The flux of this ice-rafted debris (IRD) gives researchers information about the past behavior of glaciers. As our planet warms, melting glaciers have become important drivers of sea-level rise. IRD studies can therefore help us better adapt to rising sea levels. But to do so on timescales relevant for humans, researchers have to extract thousands of samples from meters of sediment and sieve out IRD grains before manually counting them. Faster approaches would greatly ease the workload. In this study, we present a promising way to do so with the help of a medical technique: computed tomography (CT). Our findings show it is possible to semi-automatically count sand-sized grains from CT imagery without touching or destroying samples. We also show that this can be done with simple processing steps accessible to non-experts.

1. Introduction

Along glaciated margins, the calving and rafting of melting icebergs from marine-terminating glaciers deliver ice-rafted debris (IRD) to the open ocean (Ruddiman, 1977). The presence and concentration of IRD grains in marine sediment sequences provide critical information about ice sheet dynamics (Andrews, 2000). Over the past decades, such investigations have revealed enigmatic phases of millennial-scale ice sheet instability—notably Heinrich (H) events, Dansgaard-Oeschger (D-O) cycles, and Bond events (Bond et al., 1992; Dansgaard et al., 1993; Heinrich, 1988)—which have attracted significant research activity. Greater spatial coverage and a higher sampling resolution of IRD reconstructions allow us to better understand the pattern, pace, and causes of these extreme events to better assess future ice sheet stability (e.g., Hemming, 2004).

Such efforts are, however, hampered by the time-consuming laboratory work that is required to separate IRD grains from background sediments, and subsequently count individual particles. Typical steps include

multiple rounds of manually weighing, and sieving material into different grain size fractions (see e.g., Encyclopedia of Marine Geosciences, 2016 and references therein). In addition, size requirements often limit the sampling resolution of records, while the counting of split samples due to time constraints may introduce uncertainty (e.g., Van der Plas & Tobi, 1965). Evidently, (semi)-automated non-destructive approaches have significant potential to advance the field by (a) reducing analysis time, (b) improving sampling resolution, and (c) preserving valuable core material for other analyses. Over the past decades, researchers have proposed various approaches to do so, and key examples include the use of semi-automated particle size counting or the investigation of X-Ray images (Andrews et al., 1997; Becker et al., 2018; Ekblom Johansson et al., 2020; Grobe, 1987; Jennings et al., 2018). However, while the semi-automated approach (e.g., Becker et al., 2018) is destructive and requires a series of manual steps, others only target the coarsest size fraction or rely on 2-D imagery (e.g., Grobe, 1987) so that counts cannot be reported per weight or volume as is customary in the literature.

This study explores the potential of 3-D X-Ray computed tomography (CT) to overcome the aforesaid limitations. This approach distinguishes grains from host sediment based on density differences. Recent increases in resolution and sampling size have shown great promise to detect and count barely visible particles in sediment volumes (e.g., Fouinat et al., 2017; Hodell et al., 2017; Røthe et al., 2018). Here, we advance the ability of CT to semi-automatically detect and count IRD particles by (a) designing an experiment based on synthetic sediment records spiked with varying, but known, number of particles of the often-targeted 150–500 μm size fraction, (b) validating our experimental findings by comparing CT and manual particle counts on published conventionally analyzed IRD records, and (c) demonstrating that high-resolution CT counts capture high-frequency variability that is not captured by standard manual sampling protocols.

2. Materials and Methods

2.1. Experimental Design

To explore the capability of CT to detect and count IRD particles within a sediment matrix, we designed a controlled experiment using synthetic sediment archives (phantoms). For this purpose, we filled 20 standard 8 cm^3 plastic cubes with a matrix of pelagic sediment and a calculated number of grains, sieved into the 150–500 μm fraction (Figure 1a). This particular fraction was chosen as it (a) falls within an often-analyzed IRD size range, see for example (Bond et al., 1992): >150 μm, (Heinrich, 1988): 180–3,000 μm, (Hansen et al., 2015; Kanfoush et al., 2000; Murphy et al., 2002; Passchier, 2011): 150 μm to 2 mm, and (Patterson et al., 2014; St. John & Krissek, 1999): 250 μm to 2 mm, (b) excludes smaller (silt-sized) grains that may not have been ice-rafted but transported by other processes like bottom currents (e.g., Hemming, 2004; Ruddiman, 1977), and (c) can be confidently resolved from our ~21 μm resolution scans (see Section 2.3). In light of the above, we would like to emphasize that our CT-based counting method can be applied on any user-determined size fraction larger than the smallest voxel (3-D pixel) size that can be obtained with the applied scanner (see Section 2.3). Finally, to cover a broad range of IRD concentrations identified in published reconstructions, we added approximately 25, 100, 500, 1,000, and 2000 grains per gram of dry weight (g^{-1} dry sediment).

Counting three extracts of a known weight in triplicate, with the help of a Leica MZ6 optical microscope under 40× magnification, allowed us to establish a robust relation between weight and particle counts whilst quantifying the human counting error. To assess the effect of lithological differences on our results, we created four sets of phantoms that were each spiked with bedrock types that are commonly found in major IRD source areas: quartz (density of 2.65 g/cm^3), basalt (density of 3.0 g/cm^3), dolomite (density of 2.8 g/cm^3), and a 1:1:1 mixture of these materials (e.g., Bond et al., 1992; Jullien et al., 2006). For this purpose, we respectively relied on commercial quartz sand, basaltic floodplain sediments from northern Iceland (van der Bilt, Barr, et al., 2021), and a dolomite laboratory standard (see Figure S1). The mineralogy of each material was ascertained using a Bruker D8 ADVANCE ECO X-ray diffractometer, equipped with a 1.5418 Å Copper (Cu) source operated at 40 kV/25 mA (see Figure S2). As outlined above, we consider 150 μm to 2 mm grains as IRD-sized and consequently only added material retained on a 150 μm mesh, while also sieving out clasts larger than 2 mm. To assess the ability of CT data to reproduce sample grain size distributions, we determined the particle size distribution (PSD—as a normalized volume %) of each IRD-sized lithology

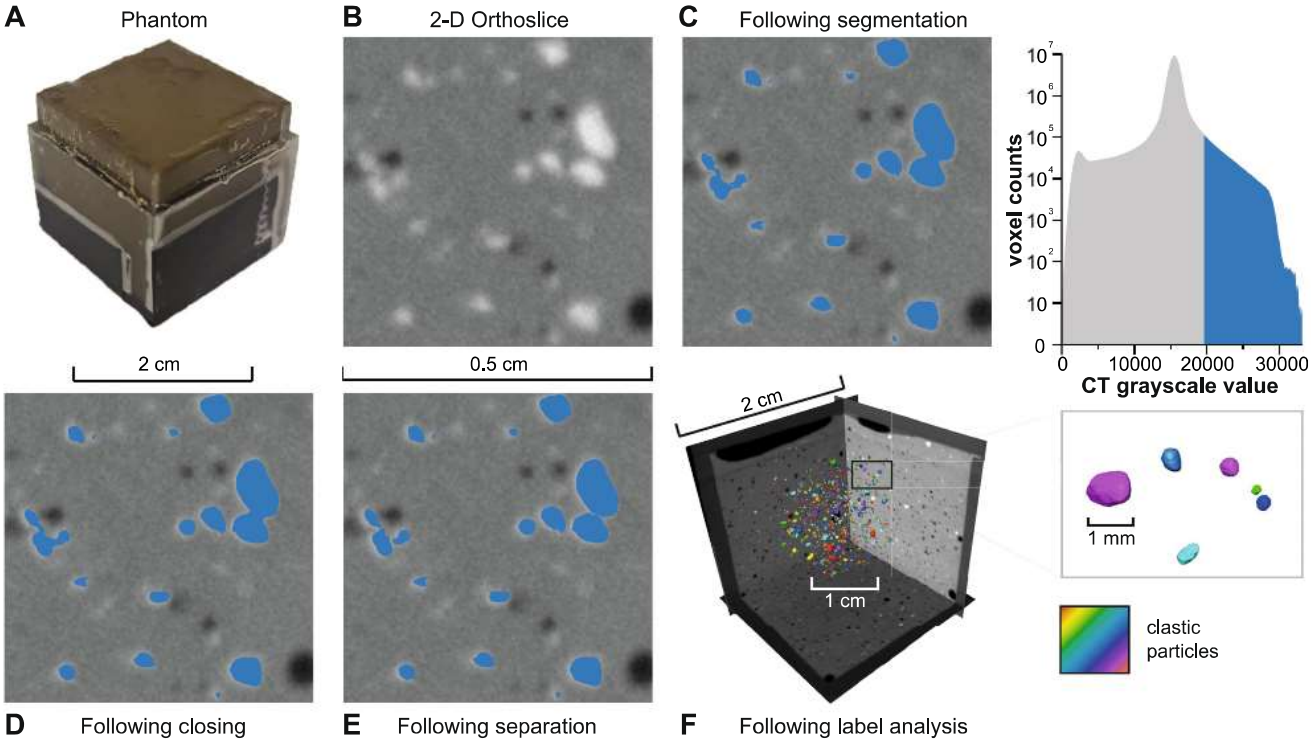

Figure 1. Imagery that highlights key steps of our experimental approach. (a) Close-up of one of the created synthetic records—phantoms. (b) A raw 0.25 cm^2 2-D cross-section (orthoslice) from one of our phantoms—note how dense radiopaque (light) clastic particles stand out. (c) Thresholded particles following iterative segmentation (see Section 2.4). The histogram on the right shows the applied CT greyscale value thresholds. (d) Restoration of fuzzy object boundaries (see Section 2.4). (e) Separation of adjoining particles. (f) Individually classified (colored) clastic particles in a 1 cm^3 3-D visualization of one of our phantoms used for subsequent digital sieving and counting.

in triplicate using a Mastersizer 3000. Samples were measured for 20 s at a stirring speed of 2,500 rpm with ultrasound applied for 40 s before measurement.

The matrix of our phantoms derives from a pelagic multi-core (GS15-198-62MC-F) retrieved off the Iceland Plateau (70°01′N 13°33′W) at 1423 m water depth (Jansen, 2015). To avoid introducing noise to the experiment, all IRD-sized particles were removed a-priori by sieving the sediment through a 63 μm mesh. Further, treatment with 1M acetic acid at 50°C (until reaction ceased) dissolved in-situ calcite shells. To each sample box, we added approximately 6 g of matrix mixed with 5 ml water to emulate the properties of natural marine sediments (see data). In addition to the aforementioned known number of IRD-sized grains, phantoms were spiked with ~600 foraminifera shells of arbitrary species larger than 150 μm from the Norwegian Sea (H. Halfidason, pers. comm.) to assess whether ubiquitous calcite shells introduce noise to CT IRD counts. The potential error margin related to loss of material during mixing and transfer of material was estimated at 0.31 g ($2\sigma = 0.61$ g), by weighing the box after finalizing it. Finally, we ascertained the Dry Bulk Density (DBD) of our phantoms after Dean Jr (1974) to convert CT-counted particles per scanned volume to particles per gram of dry weight similar to most studies.

2.2. Natural Marine Sediment Cores

To further test the potential of CT-based IRD-sized particle detection, we applied the insights gained from our phantom experiment on two published manually sieved and counted IRD stratigraphies. These encompass two segments of North Atlantic calypso cores that were extracted on-board the R/V G.O. Sars (Dokken & Cruise-Members, 2016): (a) the 454–488.5 cm segment from core GS16-204-22CC-A (58° 2.830′N, 47° 2.360′W: 3,160 m water depth), which was previously investigated by Griem et al. (2019), and (b) the 231–281 cm section of GS16-204-18CC (60° 1.840′N, 40° 33.450′W: 2,220 m water depth) (Rutledal et al., 2020).

Both segments were counted at 2 cm intervals and selected because they have been analyzed using standardized IRD wet sieving and counting methods (see Griem et al., 2019), show distinct variability, focus on the 150–500 μm size range as our experiment (Section 2.1), and the number of counted particles falls within the range of our experimental design (<2,000 IRD g^{-1} dry sediment). To optimize scanning resolution by minimizing the distance between source and detector, we extracted 2 cm wide u-channels from both sediment cores for CT scanning. As further detailed in Section 3.2, we manually recounted the 267.5–277.5 cm section of the u-channel taken from core GS16-204-18CC at 0.5 cm intervals using the same protocol applied by Griem et al. (2019). As with our phantoms (see Section 2.1), we relied on DBD measurements after Dean Jr (1974) to convert CT-derived counts per scanned volume to particles per gram dry weight. To this end, we extracted one sample near the top and bottom of the homogenous scanned section from GS16-204-22CC, while extracting four samples from the investigated segment of GS16-204-18CC due to a lithological change at 259 cm core depth as reported in Dokken and Cruise-Members (2016).

2.3. CT Scanning

Fundamentally, CT can resolve objects based on differences in X-ray absorption: X-ray photons penetrate light (black; radiolucent) materials with ease, while radiation is absorbed by dense (white; radiopaque) matter like bone (Röntgen, 1896), or clastic particles (Figure 1b). The degree of X-ray attenuation is captured by grayscale values, who typically reflect material density (higher is denser). By rotating objects or an X-ray source and detector, CT scanners generate large numbers of 2-D radiographs known as orthoslices from various angles. These images can be reconstructed to create 3-D visualizations or reconstructions (e.g., Kalender, 2011). In contrast with more established 2-D X-Ray-based IRD detection approaches (e.g., Grobe, 1987), this allows characterization and counting of particles per volume.

For this study, CT scanning was performed using a ProCon CT-ALPHA-CORE system located at the Earth Surface Sediment Laboratory (EARTHLAB) of the University of Bergen that is customized for whole-core (max. 150 cm) analysis (see e.g., van der Bilt et al., 2018). This one-of-its-kind 16-bit scanner is fitted with a 240 kV microfocus X-ray source and 9 MP detector that move vertically while the scanned object rotates. All presented scans were scanned at 800 μA and 100 kV with an exposure time of 334 ms to generate 1,600 projections per rotation. This relatively high current helps us minimize the imprint of photoelectric effect (Duliu, 1999). A physical 0.5 mm Cu filter was applied to reduce beam hardening effects (see Brooks & Di Chiro, 1976), as well as ring artifact correction and median filtering. Using 2 cm wide u-channels and boxes allowed us to optimize scanning resolution by minimizing the distance between source and detector, producing imagery at ~21 μm isotropic voxel size.

2.4. CT Processing

After scanning, CT projections were reconstructed for 3-D visualization with the Fraunhofer Volex X-ray Office software. To further minimize the imprint of CT artifacts like beam hardening or edge effects (e.g., Barrett & Keat, 2004; Section 2.4), we cropped ~1 cm^3 volumes near the center of scanned boxes and 1 cm wide sections of the u-channels. This step was performed in duplicate (henceforth referred to as samples A and B) to assess the representativeness of these 3-D cutouts. All subsequent image analyses were executed using version 9.1.1 of Thermo Scientific Avizo. To broaden the applicability of our approach, we relied on basic image processing techniques that are accessible to most geoscientists (see Figure S3). All applied tools and modules are highlighted in *italics* below and briefly described to help users execute the same steps in other often-used image processing suites like ImageJ or VGStudio Max. We first manually adjusted the visualized CT density range using the *Colormap editor* to highlight clastic particles such as IRD grains from background host sediments. This simple approach fundamentally relies on the subtle but measurable density differences between both materials and the shape of the clastic particles; as can be seen in Figure 1c, the porous (water-soaked) matrix is significantly lighter (darker) than dense (white) clasts. We then assigned a single value (1) to the designated CT density range using the *Interactive Threshold* segmentation tool. As can be seen in Figure 1b, this binary image does not adequately resolve the edge of clasts—a prerequisite when counting specific size fractions for IRD analysis. The observed noise is introduced by partial volume effects: the inter-voxel blurring of CT greyscale values along the steep density gradient between different materials (e.g., Glover & Pelc, 1980; Schlüter et al., 2010). To overcome this issue, we restored object boundaries with

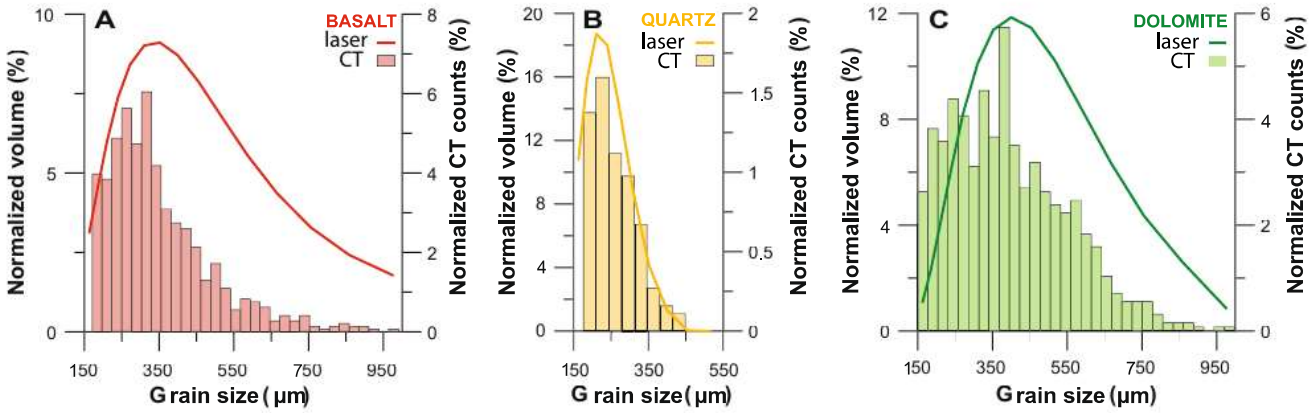

Figure 2. Comparing laser diffraction (Mastersizer: line) and computed tomography (CT)-derived (binned bars) particle size distributions (PSDs) for ice-rafted debris-sized grains of each bedrock type used to spike our phantoms: basalt (a), quartz (b), and dolomite (c). Mastersizer data are expressed as a normalized volume (%), while CT data are calculated as normalized counts (%). See Section 2.1 for additional details.

a combination of dilation and erosion using the *Closing* module as shown in Figure 1d. Next, the *Separate Objects* module was applied to make sure that adjoining or coagulating particles are split as can be seen in Figure 1e. Following the above steps to detect and resolve particles, we individually characterized them for analysis with the *Label Analysis* module (Figure 1f) based on their unique barycentric coordinates (*Bary-Center*). During this step, the equivalent diameter and shape properties of each object were also calculated using the *EqDiameter* and *Shape_Va3D* measures, respectively. We used the *Shape_Va3D* measurement to account for the fact that non-spherical objects may pass through a sieve mesh that is larger than their equivalent diameter if oriented toward their smallest projection (see e.g., Retsch, 2009). To do so, we normalized our 150 μm size threshold (see Sections 2.1 and 2.2) against the degree of non-sphericity reflected by *Shape_Va3D* values > 1. Digital sieving was performed using the *Sieve Analysis* module before summing up particle counts for each phantom and at 1 mm depth intervals in scanned core sections. Finally, we performed basic geostatistical analyses like re-sampling, correlation, and linear regression using version 16 of the StataSE software.

3. Results and Discussion

3.1. Experimental Findings

3.1.1. Particle Size Analysis

The correct identification of a known number of particles within a specific size range is of fundamental importance to this study. Therefore, we compared normalized CT particle counts on all phantoms spiked with ~1,000 grains (>150 μm) per g^{-1} dry sediment to laser diffraction-derived sample PSDs of pure extracts of each lithology used to spike these synthetic archives (Section 2.1). Both approaches rely on the equivalent diameter of a sphere with the same volume as a measure for particle size. CT counts were corrected with the *Shape_Va3D* measure to account for the possibility that non-spherical objects may pass through a sieve mesh that is larger than their equivalent diameter (see Section 2.4 and Figure S3). As can be seen in Figure 2, binned CT and laser-derived PSDs are rather similar. These findings (a) strengthen our confidence that the CT processing steps applied in this study accurately constrain the distribution of size fractions commonly targeted for IRD analysis—a prerequisite for automatic counting, (b) open doors for future venture into non-destructive CT-based particle size analysis, and (c) highlight differences between PSDs of the lithologies used to spike our phantoms to help contextualize possible counting offsets in the following paragraphs.

3.1.2. Lithic Grain Counting

As shown in Figure 3, all linear regression fits between manual and CT counts in our phantoms are highly significant (R^2 = 0.96–0.99, p = 0.00), regardless of the lithology of added grains. Besides demonstrating the potential of CT scanning to automatically count IRD-sized particles, these findings also allay concerns

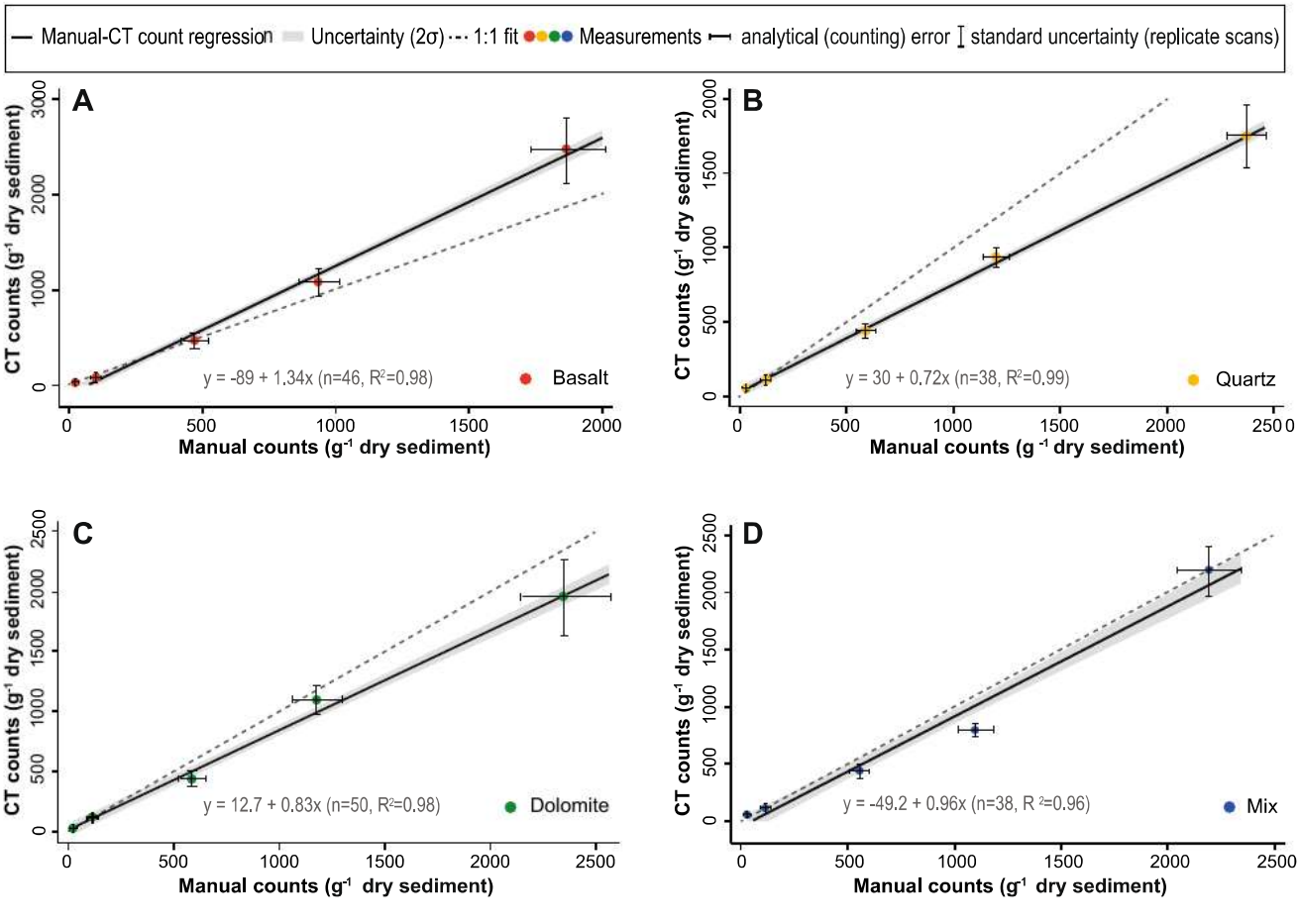

Figure 3. Linear regression fits (and summary statistics) between manual and computed tomography (CT) counts of ice-rafted debris-sized (150–500 μm) particles in synthetic sediment records (phantoms) spiked with basalt (a), quartz (b), dolomite (c), and a 1:1:1 mixture of each (d). See Section 2.1 for additional details.

that calcite shells introduce noise: the high reproducibility of lower counts in particular show that the ~600 foraminifera shells added to each phantom were not CT-counted. We attribute this to partial volume effects: while the density of calcium carbonate (2.7 g/cm^3) is near-identical to that of the rock types of added grains (2.65–3 g/cm^3), voxel blurring with air-filled, water-filled, or matrix-filled chambers of foraminiferal tests yield a lower density (Section 2.4).

Our experimental findings compare favorably with previous efforts to (semi)-automatically count particles. Fouinat et al. (2017), for example, applied a similar CT-based approach to count larger mm-scale particles in a silty matrix, but derive a poorer fit ($R^2 = 0.66$, $p = 0.015$). We argue that this weaker correspondence can be primarily attributed to a lower scanning resolution of 0.25 mm versus 21 μm in our study (Section 2.3). Becker et al. (2018) employed an approach based on automated microscopy to derive a marginally lower goodness-of-fit ($R^2 = 0.94$). However, this approach still requires destructive (lower resolution) sampling and time-consuming wet sieving.

However, while our experimental findings are promising, systematic offsets exist between manual and CT counts. While highly significant, the slopes of all fits deviate from a 1:1 relation: as seen in Figure 3, these offsets often exceed calculated counting errors (Sections 2.1 and 2.4) for all lithologies, but especially for quartz. Here, we tentatively attribute these errors to a number of analytical sources. First, differences in the PSD of lithic grains. Assuming a unimodal distribution (to estimate the proportion of sieved-out particles <150 μm—see Section 2.1), a significant percentage of grains may be included or excluded when object boundaries (and thus diameters) are incorrectly resolved during CT processing (see Section 2.4 and Figures 1c–1e). This source of error may well explain why offsets are largest for quartz as (a) the median

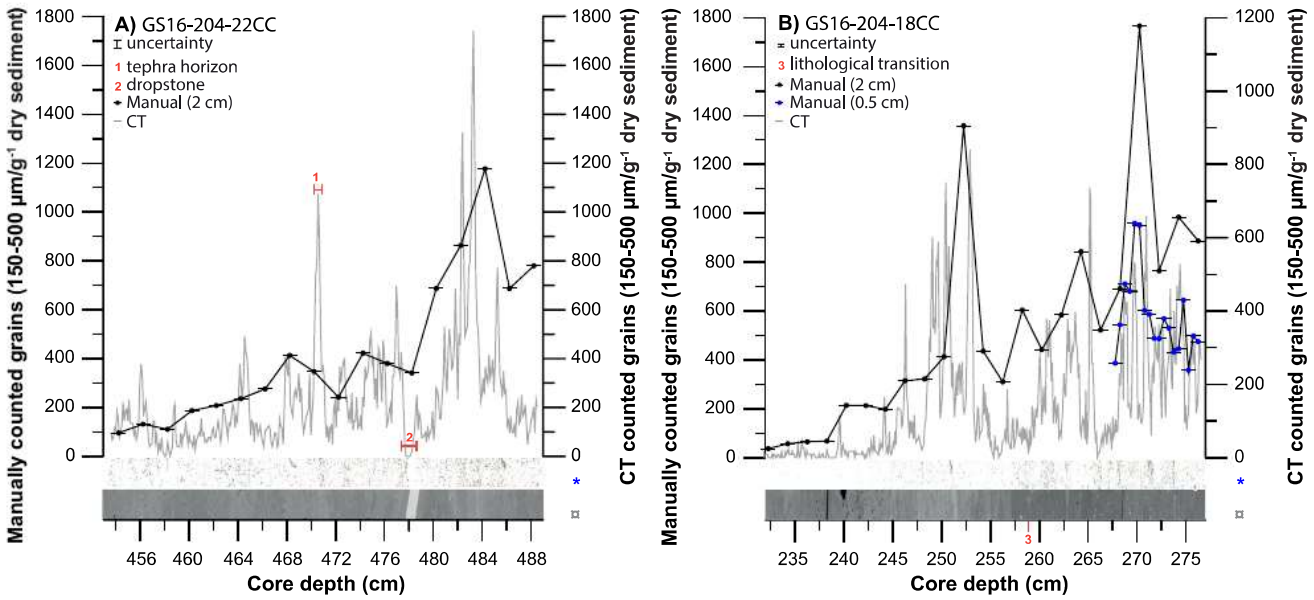

Figure 4. A comparison of manual and computed tomography (CT)-derived counts of ice-rafted debris-sized particles in two marine sediment segments. For (a) GS16-204-22CC and (b) GS16-204-18CC. Highlighted uncertainty intervals (gray) are based on the average offset in CT-derived grain counts between replicate 3-D samples A and B (see Section 2.4). Horizontal bars on manual count symbols mark the 0.5 cm sampling width (see Section 2.2). Red numerals indicate the stratigraphic position of marked features in the scanned core segments—(a) the NAAZ II tephra marker (Rutledal et al., 2020), (b) a cm-scale drop stone, and (c) a visible lithological transition (Dokken & Cruise-Members, 2016). At the base of each panel, we show CT visualizations of scanned 1 cm^3 core segments: 2-D ortho slices (lower: ¤) and 3-D visualizations of individually classified 150–500 µm grains (upper: *).

PSD of this lithology sits closest to our 150 µm cutoff (Figure 3b) so that small errors generate large count uncertainties, and (b) density differences with host sediments are smallest, which complicates our efforts to accurately resolve object boundaries based on CT greyscale values (see Section 2.4). In addition, image processing may also impact CT particle counts by erroneously splitting irregularly shaped grains into multiple objects with the *Separation* module (see Figure 1e). This source of error may help explain the observed overestimation of basaltic grains by CT counting (Figure 3a). This notion is supported by (a) visual evidence of the irregular shape of these particles (see Figure S1), and (b) their comparatively large size (Figure 2a), which increases the probability that erroneously split particles are included in the counted >150 µm fraction. The applied *Closing module* (see Section 2.4) might also have exacerbated this effect as it may expand the size of particles by smoothing uneven surfaces or filling in hollow particles (see Figures 1c and 1d).

3.2. Application on Manually Counted Natural Sediment Archives

As can be seen in Figure 4, our CT-based approach to count 150–500 µm particles capture the main IRD peaks resolved by the manually sieved and counted stratigraphies published for both cores in Griem et al. (2019) and Rutledal et al. (2020). The strength of this relation is confirmed by positive Spearman ρ values of 0.75 ($n = 18$, $p = 0.0003$) for core GS16-204-22CC and 0.63 ($n = 25$, $p = 0.0007$) for core GS16-204-18CC (Figures S4a and S4b)—all calculated on evenly (0.5 cm) resampled data. These findings clearly demonstrate the potential of our CT-based approach to semi-automatically detect the 150–500 µm-sized particles that are typically targeted in IRD studies, even at comparatively low concentrations (max. 1,800 grains/gr).

However, while certainly encouraging, the presented results also reveal substantial disparities. These can partly be explained by differences in sampling resolution: grains were CT-counted at 0.1 cm intervals, while 0.5 cm wide samples were taken every 2 cm for manual counts—smoothing out high-frequency (mm-scale) variability. As can be seen in Figure 4b, comparison with the higher 0.5 cm sampling resolution of the 267.5–277.5 cm section of our CT-scanned u-channel from core GS16-204-18CC greatly improves agreement. Indeed, correlation of both datasets using the most similar CT-derived grain numbers within the 0.5 cm sampling width of manual samples yields a Spearman ρ of 0.96 ($n = 18$, $p = 0.0000$: also see

Figure S4c)—a result that equals the robustness of our experimental findings (see Section 3.1.2). In addition, our scanned u-channel from GS16-204-22C contains two features that are also highlighted using the applied segmentation approach (see Section 2.4) due to their highly similar density: the basaltic component of a NAAZ II tephra deposit and a large drop stone (see Figure 4a: a and b). The latter is not CT-counted as its size falls outside our specified 150–500 μm grain range (see Section 2.1), but its size simply leaves less space for other particles within the 0.1 cm^3 sample slice—creating a distinct minimum in counted particles. The tephra is captured by a sharp peak in the CT-counted IRD record. To remedy this, the characteristically high concentration of particles (ash shards) in tephra deposits may be highlighted using down-core variations in CT grayscale values as outlined by van der Bilt, Cederstrøm, et al. (2021). The structural offset between CT and manual counts, which particularly affects GS16-204-18CC as seen in Figure 4b and is more difficult to account for. As both cores were counted by the same researcher and derive from the same area (see Section 2.1), we preclude differences in human counting error and lithology-specific analytical errors (see Section 3.1.2) as plausible explanations. Because the bedrock geology of proximal IRD source areas in the region is dominated by quartz-rich metamorphic bedrock types (Dawes, 2009), it is worth noting that the offset between evenly sampled CT and manual counts in GS16-204-22CC is identical (28%) to the difference found in our quartz-spiked phantoms (Figure 3b). But why this mismatch far greater in GS16-204-18CC, where our CT-based approach captures just 40% of manually counted grains (Figure 4b)? We argue that the dissimilarity between both datasets may be attributed to disturbance introduced by bioturbation. In recent years, numerous researchers have harnessed various imaging techniques to demonstrate that burrowing may modify the sediment structure and blur IRD signals (e.g., Dorador et al., 2014; Hodell et al., 2017). Indeed, Rutledal et al. (2020) relied on the same threshold-based segmentation routine presented in Section 2.4 to highlight the presence of burrows filled with air or water in GS16-204-18CC and GS16-204-22CC. As can be seen in Figure S5, these features appear particularly extensive in the section of GS16-204-18CC scanned for this study. Closer inspection of the X-Ray images shown in Figure S5, using histogram equalization of CT imagery as suggested by Miguez-Salas et al. (2019), also highlights the presence of infilled burrows. Because these features are distributed vertically (depth: z) as well as horizontally (width: y) along split core surfaces–as can be seen in Fig. s5 – bioturbation redistributes IRD grains in both these directions. As there is a 1–2 cm y-offset between the manual sampling locations and scanned CT u-channels in the investigated section of core GS16-204-18CC, this reworking process may help explain the offsets between manual and CT-derived count profiles. To test this, we compared our CT data from GS16-204-18CC to the higher-resolution (0.5 cm) manual counts performed on the same scanned u-channel (see Section 2.2). As can be seen in Figure 4b, the offset between these data is significantly smaller and rather similar (39%) to the difference found between counts and scans in our quartz-spiked phantoms (28%). Following from the above, we argue that our work supports other recent CT-derived evidence that bioturbation can extensively rework IRD profiles.

4. Conclusions

This study underscores the potential of CT scanning for semi-automated and non-destructive counting of IRD-sized grains in sediment archives. Notwithstanding analytical errors that we ascribe to image processing artifacts, our experimental findings show that CT numbers capture more than 95% of grain count variability in homogenous phantoms. Also, by spiking each of these synthetic samples with a known number of foraminiferal tests, we allay concerns that (often-ubiquitous) calcite shells of a similar size and density affect CT IRD counts. Despite evidence of bioturbation and differences in sampling resolution, CT-derived counts strongly correlate ($\rho = 0.63$–0.75) with manual IRD profiles in both scanned core sections. Moreover, quadrupling our manual counting resolution on CT-scanned u-channels minimizes offsets between both datasets ($\rho = 0.96$). This somewhat surprising result suggests that mm-scale CT variations capture a signal rather than noise and highlights how bioturbation may rework IRD profiles. Importantly, all our results were acquired using basic image processing techniques that can be quickly mastered by most geologists. Following from the above, we argue that the presented CT-based counting approach significantly benefit IRD investigations by preserving material, improving sampling resolution, and optimizing lab workflows. By enabling faster detection of higher-frequency IRD events, these advances have significant potential to deepen our understanding of climate-ice sheet interactions on human-relevant timescales.

Data Availability Statement

The authors have archived all numerical data presented in the main manuscript in the Dataverse repository, and these will be made available upon publication. For now, the authors have attached a copy of this file as Supporting Information S1 for review purposes.

Acknowledgments
The authors want to express our gratitude to the Trond Mohn Foundation and the Centre for Climate Dynamics for funding this research through their Starting Grant and Fast-Track initiative programs, respectively. The authors also acknowledge support from the European Research Council under the European Community's Seventh Framework Program (FP7/2007-2013)/ERC grant agreement 610055 as part of the Ice2ice project. Finally, the authors want to thank Lisa Griem for providing manually counted IRD profiles for the scanned core segments, and Rick Hennekam as well as Eystein Jansen for helping us improve this manuscript with their comments.

References

Andrews, J., Smith, L., Preston, R., Cooper, T., & Jennings, A. (1997). Spatial and temporal patterns of iceberg rafting (IRD) along the East Greenland margin, ca. 68 N, over the last 14 cal. ka. *Journal of Quaternary Science: Published for the Quaternary Research Association*, *12*(1), 1–13. https://doi.org/10.1002/(sici)1099-1417(199701/02)12:1<1::aid-jqs288>3.0.co;2-t

Andrews, J. T. (2000). Icebergs and iceberg rafted detritus (IRD) in the North Atlantic: Facts and assumptions. *Oceanography*, *13*, 100–108. https://doi.org/10.5670/oceanog.2000.19

Barrett, J. F., & Keat, N. (2004). Artifacts in CT: Recognition and avoidance. *RadioGraphics*, *24*(6), 1679–1691. https://doi.org/10.1148/rg.246045065

Becker, L. W., Hjelstuen, B. O., Støren, E. W., & Sejrup, H. P. (2018). Automated counting of sand-sized particles in marine records. *Sedimentology*, *65*(3), 842–850. https://doi.org/10.1111/sed.12407

Bond, G., Heinrich, H., Broecker, W., Labeyrie, L., McManus, J., Andrews, J., et al. (1992). Evidence for massive discharges of icebergs into the North Atlantic Ocean during the last glacial period. *Nature*, *360*(6401), 245–249. https://doi.org/10.1038/360245a0

Brooks, R. A., & Di Chiro, G. (1976). Beam hardening in x-ray reconstructive tomography. *Physics in Medicine and Biology*, *21*(3), 390–398. https://doi.org/10.1088/0031-9155/21/3/004

Dansgaard, W., Johnsen, S. J., Clausen, H. B., Dahl-Jensen, D., Gundestrup, N., Hammer, C., et al. (1993). Evidence for general instability of past climate from a 250-kyr ice-core record. *Nature*, *364*(6434), 218–220. https://doi.org/10.1038/364218a0

Dawes, P. R. (2009). The bedrock geology under the Inland Ice: The next major challenge for Greenland mapping. *Geological Survey of Denmark and Greenland Bulletin*, *17*, 57–60.

Dean, W. E., Jr. (1974). Determination of carbonate and organic matter in calcareous sediments and sedimentary rocks by loss on ignition: Comparison with other methods. *Journal of Sedimentary Research*, *44*(1). https://doi.org/10.1306/74d729d2-2b21-11d7-8648000102c1865d

Dokken, T. M., & Cruise-Members. (2016). *Cruise report of cruise GS16-204 (Reykjavik-Narsarsuaq)*. Retrieved from https://www.bcdc.no/files/bcdc-theme/documents/GS16-204_cruise%20report.pdf

Dorador, J., Rodríguez-Tovar, F. J., & Expedition, I. (2014). Quantitative estimation of bioturbation based on digital image analysis. *Marine Geology*, *349*, 55–60. https://doi.org/10.1016/j.margeo.2014.01.003

Duliu, O. G. (1999). Computer axial tomography in geosciences: An overview. *Earth-Science Reviews*, *48*(4), 265–281. https://doi.org/10.1016/s0012-8252(99)00056-2

Ekblom Johansson, F., Wangner, D. J., Andresen, C. S., Bakke, J., Støren, E. N., Schmidt, S., & Vieli, A. (2020). Glacier and ocean variability in Ata Sund, west Greenland, since 1400 CE. *The Holocene*, *30*(12), 1681–1693. https://doi.org/10.1177/0959683620950431

Encyclopedia of Marine Geosciences. (2016). Dordrecht: Springer.

Fouinat, L., Sabatier, P., Poulenard, J., Reyss, J.-L., Montet, X., & Arnaud, F. (2017). A new CT scan methodology to characterize a small aggregation gravel clast contained in a soft sediment matrix. *Earth Surface Dynamics*, *5*(1), 199–209. https://doi.org/10.5194/esurf-5-199-2017

Glover, G., & Pelc, N. (1980). Nonlinear partial volume artifacts in x-ray computed tomography. *Medical Physics*, *7*(3), 238–248. https://doi.org/10.1118/1.594678

Griem, L., Voelker, A. H., Berben, S. M., Dokken, T. M., & Jansen, E. (2019). Insolation and glacial meltwater influence on sea-ice and circulation variability in the Northeastern Labrador sea during the Last Glacial Period. *Paleoceanography and Paleoclimatology*, *34*(11), 1689–1709. https://doi.org/10.1029/2019pa003605

Grobe, H. (1987). A simple method for the determination of ice-rafted debris in sediment cores. *Polarforschung*, *57*(3), 123–126. https://doi.org/10.1080/1046171x.1987.12034306

Hansen, M. A., Passchier, S., Khim, B. K., Song, B., & Williams, T. (2015). Threshold behavior of a marine-based sector of the East Antarctic Ice Sheet in response to early Pliocene ocean warming. *Paleoceanography*, *30*(6), 789–801. https://doi.org/10.1002/2014pa002704

Heinrich, H. (1988). Origin and consequences of cyclic ice rafting in the northeast Atlantic Ocean during the past 130,000 years. *Quaternary Research*, *29*(2), 142–152. https://doi.org/10.1016/0033-5894(88)90057-9

Hemming, S. R. (2004). Heinrich events: Massive late Pleistocene detritus layers of the North Atlantic and their global climate imprint. *Reviews of Geophysics*, *42*(1). https://doi.org/10.1029/2003rg000128

Hodell, D. A., Nicholl, J. A., Bontognali, T. R., Danino, S., Dorador, J., Dowdeswell, J. A., et al. (2017). Anatomy of Heinrich Layer 1 and its role in the last deglaciation. *Paleoceanography*, *32*(3), 284–303. https://doi.org/10.1002/2016pa003028

ICCD. (2007). *PDF-2, database sets 1–45*. International Centre for Diffraction Data.

Jansen, E. (2015). *Cruise report of cruise GS15-198*. Reykjavik-Tromsø.

Jennings, A. E., Andrews, J. T., Cofaigh, C. Ó., St-Onge, G., Belt, S., Cabedo-Sanz, P., et al. (2018). Baffin Bay paleoenvironments in the LGM and HS1: Resolving the ice-shelf question. *Marine Geology*, *402*, 5–16. https://doi.org/10.1016/j.margeo.2017.09.002

Jullien, E., Grousset, F. E., Hemming, S. R., Peck, V. L., Hall, I. R., Jeantet, C., & Billy, I. (2006). Contrasting conditions preceding MIS3 and MIS2 Heinrich events. *Global and Planetary Change*, *54*(3–4), 225–238. https://doi.org/10.1016/j.gloplacha.2006.06.021

Kalender, W. A. (2011). *Computed tomography: Fundamentals, system technology, image quality, applications*. John Wiley & Sons.

Kanfoush, S. L., Hodell, D. A., Charles, C. D., Guilderson, T. P., Mortyn, P. G., & Ninnemann, U. S. (2000). Millennial-scale instability of the Antarctic ice sheet during the last glaciation. *Science*, *288*(5472), 1815–1819. https://doi.org/10.1126/science.288.5472.1815

Miguez-Salas, O., Dorador, J., & Rodríguez-Tovar, F. J. (2019). Introducing Fiji and ICY image processing techniques in ichnological research as a tool for sedimentary basin analysis. *Marine Geology*, *413*, 1–9. https://doi.org/10.1016/j.margeo.2019.03.013

Murphy, L., Warnke, D., Andersson, C., Channell, J., & Stoner, J. (2002). History of ice rafting at South Atlantic ODP Site 177-1092 during the Gauss and late Gilbert Chrons. *Palaeogeography, Palaeoclimatology, Palaeoecology*, *182*(3–4), 183–196. https://doi.org/10.1016/s0031-0182(01)00495-3

Passchier, S. (2011). Linkages between East Antarctic Ice Sheet extent and Southern Ocean temperatures based on a Pliocene high-resolution record of ice-rafted debris off Prydz Bay, East Antarctica. *Paleoceanography*, *26*(4). https://doi.org/10.1029/2010pa002061

Patterson, M. O., McKay, R., Naish, T., Escutia, C., Jimenez-Espejo, F., Raymo, M., et al. (2014). Orbital forcing of the East Antarctic ice sheet during the Pliocene and Early Pleistocene. *Nature Geoscience*, *7*(11), 841–847. https://doi.org/10.1038/ngeo2273

Retsch, G. (2009). *Sieve analysis taking a close look quality*.

Röntgen, W. C. (1896). On a new kind of rays. *Science*, *3*(59), 227–231. https://doi.org/10.1126/science.3.59.227

Røthe, T. O., Bakke, J., Støren, E. W., & Bradley, R. S. (2018). Reconstructing Holocene glacier and climate fluctuations from lake sediments in Vårfluesjøen, northern Spitsbergen. *Frontiers of Earth Science*, *6*.

Ruddiman, W. F. (1977). Late Quaternary deposition of ice-rafted sand in the subpolar North Atlantic (lat 40 to 65 N). *The Geological Society of America Bulletin*, *88*(12), 1813–1827. https://doi.org/10.1130/0016-7606(1977)88<1813:lqdois>2.0.co;2

Rutledal, S., Berben, S. M., Dokken, T. M., Van Der Bilt, W. G., Cederstrøm, J. M., & Jansen, E. (2020). Tephra horizons identified in the western North Atlantic and Nordic Seas during the Last Glacial Period: Extending the marine tephra framework. *Quaternary Science Reviews*, *240*, 106247. https://doi.org/10.1016/j.quascirev.2020.106247

Schlüter, S., Weller, U., & Vogel, H.-J. (2010). Segmentation of X-ray microtomography images of soil using gradient masks. *Computers & Geosciences*, *36*(10), 1246–1251. https://doi.org/10.1016/j.cageo.2010.02.007

St John, K. E., & Krissek, L. A. (1999). Regional patterns of Pleistocene ice-rafted debris flux in the North Pacific. *Paleoceanography*, *14*(5), 653–662. https://doi.org/10.1029/1999pa900030

van der Bilt, W. G., Barr, I. D., Berben, S. M., Hennekam, R., Lane, T., Adamson, K., & Bakke, J. (2021). Late Holocene canyon-carving floods in northern Iceland were smaller than previously reported. *Communications Earth & Environment*, *2*(1), 1–12. https://doi.org/10.1038/s43247-021-00152-4

van der Bilt, W. G., Cederstrøm, J., Støren, E., Berben, S., & Rutledal, S. (2021). Rapid tephra identification in geological archives with computed tomography: Experimental results and natural applications. *Frontiers of Earth Science*, *8*, 622386. https://doi.org/10.3389/feart.2020.622386

van der Bilt, W. G., Rea, B., Spagnolo, M., Roerdink, D., Jørgensen, S., & Bakke, J. (2018). Novel sedimentological fingerprints link shifting depositional processes to Holocene climate transitions in East Greenland. *Global and Planetary Change*. https://doi.org/10.1016/j.gloplacha.2018.03.007

Van der Plas, L., & Tobi, A. (1965). A chart for judging the reliability of point counting results. *American Journal of Science*, *263*(1), 87–90. https://doi.org/10.2475/ajs.263.1.87